JOURNAL OF AIRCRAFT
Vol. 29, No. 5, Sept.–Oct. 1992

Viscous Flow Simulation of a Fighter Aircraft

Oh. J. Kwon*
Sverdrup Technology, Inc., Brook Park, Ohio 44135
and
Lakshmi N. Sankar†
Georgia Institute of Technology, Atlanta, Georgia 30332

A computer code capable of solving the three-dimensional compressible, unsteady, Navier-Stokes equations has been developed. This solver has been applied to steady and unsteady subsonic flow past highly swept wings and wing-body-inlet combinations at high angles of attack. Calculations for isolated wings show the formation of a leading-edge vortex. At sufficiently high angles of attack, the lift distribution over the wing begins to oscillate in time. Calculations for wings subjected to a ramp motion reveal substantially higher lift loads prior to stall than for the static fixed angle-of-attack conditions. The results for wing-body-inlet combinations show separated flow off the sharp inlet leading edge, vortex formation over wing-inlet interface region, and over the wing leading edge. The vortex core trajectory and the flowfield agree well qualitatively with the experimental results. The analysis shows near-periodic fluctuations in the sectional lift coefficients with time. A Fourier analysis of the sectional lift coefficients reveals the flowfield to be rich in discrete frequencies. Calculations have also been carried out for a vertical tail configuration, which indicates large lateral forces on the vertical tail due to interaction between the vertical tail and the vortical flow off the wing-body-inlet configuration.

Introduction

DURING the past 10 years, combat aircraft designers have developed increasingly sophisticated fighter aircraft such as the F-14, F-15, and the F-16 that are capable of performing subsonic and transonic maneuvers at high angles of attack. During the high-angle-of-attack maneuvers, the flow inevitably separates over the highly swept wing leading edge forming vortical flows. The formation of this flow phenomena has both beneficial and adverse effects on the aircraft performance. The vortex will lead to low pressures over the wing upper surface and enhance the lift that the wing is capable of generating from an otherwise attached flow. This additional lift, known as the "vortex lift," may be used to perform the required maneuver. Under certain conditions, however, this vortex may burst or be shed leading to adverse effects such as wing-rock phenomena, wing-vortex-tail interaction, and stall. Twin vertical tail aircraft such as the F-15 and F-18 are particularly vulnerable to vortex-vertical tail interactions that can cause component failure due to excessive airloads, vibrations, and fatigue.

Until recently, it was difficult to predict these phenomena, and quantitatively estimate the airloads on the aircraft during high-angle-of-attack maneuvers. Designers relied on costly wind-tunnel studies and flight tests, or on lower order incompressible flow based potential flow formulations to understand these phenomena. During the 1980s, developments in Computational Fluid Dynamics (CFD) algorithms, improvements in automated grid generation techniques and advancements in computer technology came into place. As a result, researchers have begun to perform high angle-of-attack aerodynamics studies of fighter aircraft.[1,2]

The purpose of the present investigation is to apply an existing Navier-Stokes computer code to predict the subsonic separated flow past fighter wings and wing-body-inlet configurations at high angles of attack. The interaction between the vertical tail and the vortical flow off the wing-body-inlet configuration has also been studied. The algorithm used is a finite difference procedure that is first- or second-order accurate in time, and second- or fourth-order accurate in space. A semi-implicit time marching scheme is used to integrate the equations. The computer code has been structured so that the numerically intensive portions of the flow solver take advantage of the vector processors on the current generation of supercomputers. This allows computationally intensive calculations involving several hundred thousand node points and several thousand time-steps to be performed in an efficient manner. This flow solver has been previously used to study steady and unsteady transonic flow past fighter wings,[3] helicopter rotors,[4] high-speed propellers,[5] and wing-body configurations.[6]

Mathematical and Numerical Formulation

The three-dimensional unsteady, compressible Reynolds-averaged Navier-Stokes equations may formally be written as

$$\boldsymbol{q}_t + \boldsymbol{F}_x + \boldsymbol{G}_y + \boldsymbol{H}_z = R_x + S_y + T_z \qquad (1)$$

Here $\boldsymbol{q}$ is vector containing the unknown flow properties such as density, velocity, and temperature. The quantities $\boldsymbol{F}$, $\boldsymbol{G}$, and $\boldsymbol{H}$ are inviscid flux vectors and contain information related to the convective transport of mass, momentum, energy, and pressure forces. The terms R, S, and T contain viscous (laminar and turbulent) stress contributions to mass, momentum, and energy transport.

To facilitate the computation of flow past arbitrary-shaped configurations such as wings and wing-body combinations, and to account for the motion of these surfaces during maneuvers these equations are transformed to a new coordinate system τ, ξ, η, ζ, in which the solid surfaces such as the wing or fuselage maps onto surfaces such as ξ = constant or η = constant. In such a coordinate system, the governing equations may formally be written as

$$\boldsymbol{q}_\tau + \boldsymbol{F}_\xi + \boldsymbol{G}_\eta + \boldsymbol{H}_\zeta = \boldsymbol{R}_\xi + \boldsymbol{S}_\eta + \boldsymbol{T}_\zeta \qquad (2)$$

Presented as Paper 91-0278 at the AIAA 29th Aerospace Sciences Meeting, Reno, NV, Jan. 7–10, 1991; received May 4, 1991; revision received Aug. 5, 1991; accepted for publication Aug. 5, 1991.

*Postdoctoral Fellow, School of Aerospace Engineering. Member AIAA.

†Associate Professor, School of Aerospace Engineering. Member AIAA.

The quantities $\boldsymbol{q}, \boldsymbol{F}, \boldsymbol{G}, \boldsymbol{H}$, and so on depend on their Cartesian counterparts q, F, G, and H through the metrics of transformation, and are listed in detail in Ref. 4.

The objective of calculation is then to integrate these equations numerically, starting from an initial guess for the flow vector $\boldsymbol{q}$, by marching in time. At every time-step, appropriate boundary conditions for the flow properties must be imposed. In viscous flows, the appropriate boundary conditions are that the fluid and solid have the same velocity, and that the temperature and density gradients vanish at the solid surface. At the boundaries sufficiently far away from the solid surfaces, the flow properties have been assumed to return to their uniform freestream flow conditions.

A finite-difference procedure has been used to approximate the various derivatives appearing in Eq. (2). Although second-order and fourth-order accuracy in space are possible with the present formulation, for the sake of clarity only the simplest first-order temporal, second-order spatial formulation is described here. The finite-difference analog of Eq. (2) at a time level n is then

$$\Delta \boldsymbol{q}^{n+1}/\Delta t + \delta_\xi \boldsymbol{F}^{n+1} + \delta_\eta \boldsymbol{G}^* + \delta_\zeta \boldsymbol{H}^{n+1} = (\delta_\xi \boldsymbol{R} + \delta_\eta \boldsymbol{S} + \delta_\zeta \boldsymbol{T})^n \tag{3}$$

Here δ_ξ, δ_η, and δ_ζ are standard symmetric central-difference operators. The quantity Δq^{n+1} is the change in $\boldsymbol{q}$ during adjacent time levels and Δt is the time-step. Note that the viscous terms at the right side are evaluated explicitly (at the previous time level n) while the quantities $\boldsymbol{F}$ and $\boldsymbol{H}$ are evaluated implicitly at the new time level $n + 1$. The spanwise derivative $\delta_\eta \boldsymbol{G}^*$ is evaluated semi-implicitly, that is using old time-level values and new time-level values as they become available.

Equation (3), in its present form, is a set of nonlinear algebraic equations for the change in flow property $\Delta \boldsymbol{q}$. In order to solve for $\Delta \boldsymbol{q}$, the nonlinear vectors $\boldsymbol{F}$ and $\boldsymbol{H}$ at new time level $n + 1$ are linearized at every time level about their values at the previous time level n as follows:

$$\boldsymbol{F}^{n+1} = \boldsymbol{F}^n + A^n \Delta \boldsymbol{q}^{n+1} \tag{4a}$$

$$\boldsymbol{H}^{n+1} = \boldsymbol{H}^n + B^n \Delta \boldsymbol{q}^{n+1} \tag{4b}$$

where A is a 5×5 matrix, given by $\partial \boldsymbol{F}/\partial \boldsymbol{q}$, and B is $\partial \boldsymbol{H}/\partial \boldsymbol{q}$, evaluated at time level n.

The linearized system of algebraic equations may be formally written in the following operator form, as a system of equations involving the unknown $\Delta \boldsymbol{q}$:

$$[I + \Delta t \delta_\xi A + \Delta t \delta_\zeta B]\{\Delta \boldsymbol{q}\}^{n+1} = \boldsymbol{R}^{n,n+1} \tag{5}$$

where I is the identity matrix and the right-hand side $\boldsymbol{R}$ is the residual containing all the necessary known information from the previous time level about $\boldsymbol{F}, \boldsymbol{G}, \boldsymbol{H}, \boldsymbol{R}, \boldsymbol{S}$, and $\boldsymbol{T}$. In steady-state applications, a solution to the three-dimensional Navier-Stokes equations requires that this quantity $\boldsymbol{R}$ be driven to zero in an iterative fashion. In an unsteady problem, $\boldsymbol{R}$ is of the order of the time-step Δt and need not necessarily go to zero after a sufficiently large number of time-steps.

Equation (5) couples the quantity $\Delta \boldsymbol{q}$ at every point in the flowfield with its four neighbor nodes, and is a block pentadiagonal system. A direct inversion of the pentadiagonal system is costly, and some type of approximation is required to reduce the CPU time. The conventional techniques require strategies such as incomplete LU decomposition, or an alternating direction approximate factorization AF. The AF scheme is used here, and requires factorization of the matrix operator on the left side of Eq. (5) into two smaller operators, leading to the solution of the following equation:

$$[I + \Delta t \delta_\xi A][I + \Delta t \delta_\zeta B]\{\Delta \boldsymbol{q}\}^{n+1} = \boldsymbol{R}^{n,n+1} \tag{6}$$

It may be shown that Eq. (6) requires solving at every node two tridiagonal matrix equations rather than a single pentadiagonal matrix equation. Solution of tridiagonal matrix systems may be performed efficiently using the well-known Thomas algorithm,[7] and may also be easily vectorized.

The above temporal differencing scheme is called a hybrid time differencing scheme, and has several advantages over fully explicit schemes and fully implicit schemes. The flow property vector $\boldsymbol{q}$ needs to be stored at only one time level. Most schemes require the flow properties (or changes in $\boldsymbol{q}$) to be stored at several time levels. Thus, the present approach is memory-efficient. The above scheme requires a single evaluation of the residual at a node per time-step, and two tridiagonal matrix inversions. Fully explicit schemes require residual calculations to be performed two or four times per node per time-step. Fully implicit schemes require three tridiagonal matrix inversions and are computationally expensive. The present approach can be coded such that the flow variables at five η = constant planes need be in memory at a given time. Flow variables at the other planes may reside on secondary storage devices. Thus, this approach works well on virtual memory machines.

In high Reynolds number flows, use of standard central differences can cause oscillations to appear at every time-step. These high-frequency spatial oscillations can grow if unchecked, and can lead to catastrophic failure of the solution. To avoid this, at every time-step, the solution is smoothed using a weighted formula linking a node to its four neighbors. For enhanced stability, the correction $\Delta \boldsymbol{q}$ is also smoothed. In viscous flows, it is necessary to augment the laminar viscosity coefficient with an eddy viscosity coefficient using the Baldwin-Lomax algebraic turbulence model. Because the present work deals with fully separated flows at high angles of attack, the flow is assumed to be turbulent everywhere and no transition from laminar to turbulent flow was specified. For details on the implementation of these smoothing operations, and details on the computation of the turbulence model used in the calculations, the reader is referred to Ref. 4.

Results and Discussion

The present calculations may be divided into three categories. First, several wing-alone calculations at steady-state and a rapid pull-up maneuver of the wing were done. Then, a wing-body-inlet calculation was performed. The wing-alone analysis provides a baseline analysis. By comparing the wing-alone calculations with the wing-body-inlet calculations, it is possible to determine if components such as the fuselage, inlet, and gun bump significantly influence the vortical field over the wing. Finally, the wing-body-inlet analysis serves as the input to the vertical stabilizer analysis, and the side forces over the vertical stabilizer due to the vortical flow over the wing-body-inlet combination were estimated. The Reynolds number for the calculations was 1.5 million. All the calculations here were done in a time-accurate mode, requiring approximately 20 μs/grid/time-step on a typical Cray-Y/MP machine.

The geometry being modeled is that of an F-15 aircraft. The aircraft surface definition is based on the input data set to a panel method in use at the Wright Patterson Air Force Base. The vertical tail was removed from the geometry (and modeled separately using a wing-alone analysis). The horizontal tail was not modeled. The inlet was faired over. A body-fitted grid over the resulting configuration was generated using a three-dimensional Thompson-Thames-Mastin type grid generator developed by the present authors. The wing and fuselage geometry data were enriched using cubic interpolation in the streamwise direction and linear interpolation in the span direction within the grid generator. The resulting grid was of C-H topology with 131 points in the wrap-around direction (50 points on the upper surface, 50 points on the lower surface), 38 points in the spanwise diretion of which 33

points are on the body surface, and 45 points in the normal direction. Figure 1 shows the surface grids of the wing-body-inlet configuration. Figure 2 shows the grid system at the fuselage symmetric plane. The body-fitted grid around the wing for wing-alone analysis and the vertical tail was a C-H grid, generated using the same grid generator with 121 points in the wrap-around direction, 14 points in the spanwise direction, and 45 points in the normal direction. Thus, the wing-body-inlet and vertical tail grids together have a total of 327,465 nodes surrounding half of the aircraft. The normal spacing was fairly coarse (approximately 0.001 times the fuselage length). Thus, the present grid will not accurately resolve the boundary layer over the attached regions, but is adequate enough to model leading-edge flow separation properly, and for the capture of the vortical flow over the wing. The downstream, upstream, and lateral boundaries of the grids were approximately six body lengths away from the surface.

Wing-Alone Calculations

Wing-alone calculations were performed for several angles of attack (20, 25, and 30 deg angles of attack at steady state and a rapid pull-up maneuver). Figure 3 shows typical results for the F-15 wing at 0.15 Mach number and 25-deg angle of attack. Trajectories of inert particles introduced into the flow at steady state are shown. The particles injected into the core of the vortex are seen to follow a helical trajectory, and the helical path gradually diverges, indicating a growth in the vortex structure as the particles are convected from the leading edge to trailing edge. Particles introduced outside the vortex are seen to be swept by the vortex over the wing, and then convected downstream. For this condition, the vortex has not burst, and fairly high values of lift are achieved due to the presence of the vortex. When the angle of attack is increased, however, the calculations at 30-deg angle of attack reveal that the vortex bursts, leading to stall. The chordwise location, where vortex burst occurs, moves upstream with angle of attack. Figure 4 shows the flattening out of the lift as angle of attack is increased.

Figure 4 also shows the computed sectional lift coefficients for a second case, for the F-15 wing subjected to a linear pitch up from 0-deg angle of attack to 45 deg over a period of time at a pitch rate of 0.55 rad/s. This calculation simulates a rapid pull up maneuver of a fighter aircraft. It is seen that during this maneuver, substantially high values of lift result, and stall is postponed past 35 deg.

When the angle of attack is sufficiently high, the lift distribution over the wing begins to oscillate, as shown in Fig. 5. An examination of these loads using classical Fourier series techniques reveals, as shown in Fig. 6, that the lift time history is rich with discrete frequencies corresponding to 15, 30, and 45 Hz and higher-order interactions, when the length scale and velocity scale are based on the full-size aircraft at M_∞ = 0.15 under sea level conditions. At higher frequencies, the

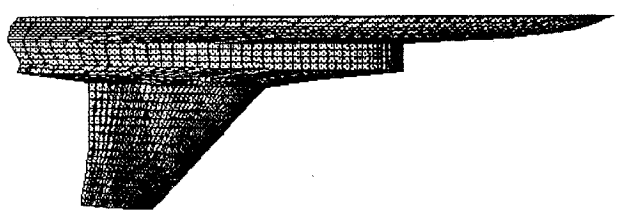

a) Top view

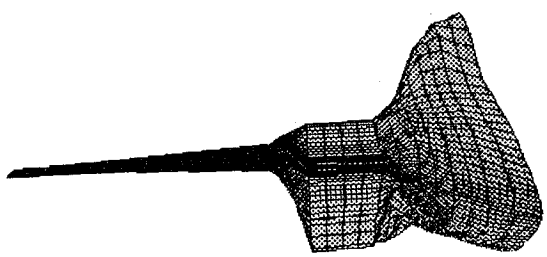

b) Front view

Fig. 1 Surface grid distribution on the wing-body-inlet configuration.

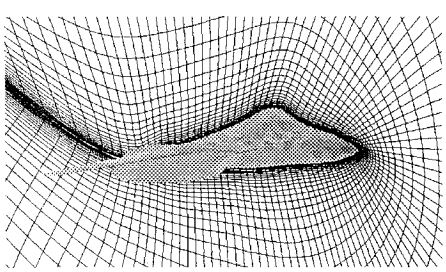

Fig. 2 Typical C-H grid topology around the wing-body-inlet configuration.

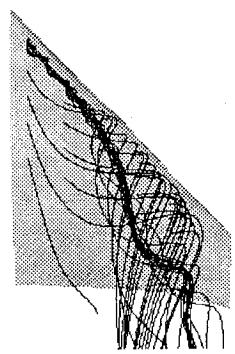

a) Top view

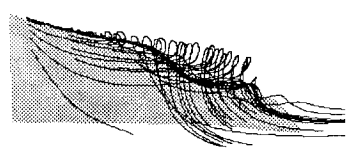

b) Rear view

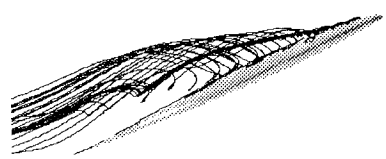

c) Side view

Fig. 3 Particle trajectories of flow over an F-15 wing-alone configuration at M_∞ = 0.15 and α = 25 deg.

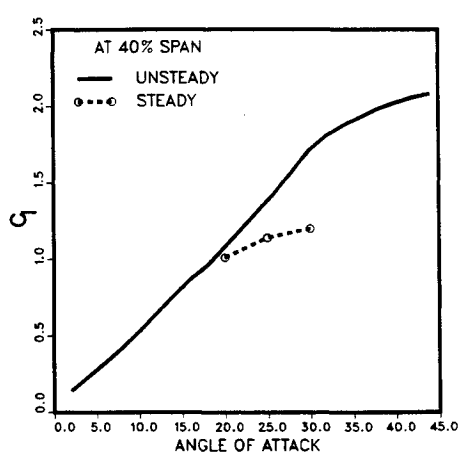

Fig. 4 Variation of sectional lift coefficient with angle of attack for the wing-alone configuration at M_∞ = 0.15.

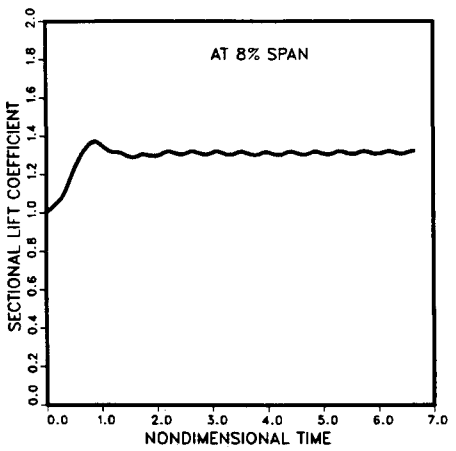

Fig. 5 Variation of sectional lift coefficient with time for the wing-alone configuration at $M_\infty = 0.15$ and $\alpha = 25$ deg.

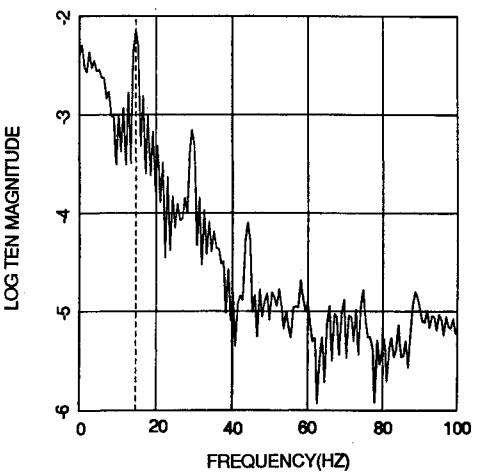

Fig. 6 Fourier transform of sectional lift coefficient for conditions shown in Fig. 5.

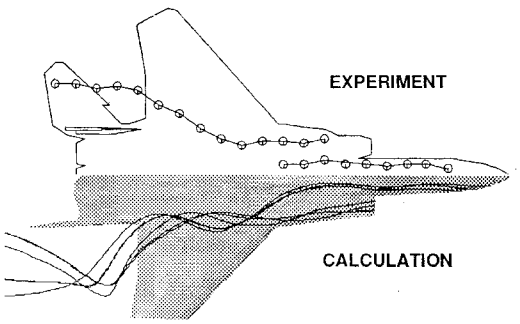

Fig. 7 Particle trajectories for flow over an F-15 wing-body-inlet configuration at $M_\infty = 0.15$ and $\alpha = 20$ deg (top view).

expected drop-off in the information content occurs in a logarithmic fashion.

Wing-Body-Inlet Analyses

Figures 7 and 8 display the particle trajectories for a wing-body-inlet combination at 20-deg angle of attack. The approximate trajectory of the vortex core obtained from the calculation is also compared with the experiment obtained from flow visualization studies.[8] It is seen that the flow over the aircraft forebody and inlet is completely separated and generates vortical flows, which eventually merge together and form a strong vortex over the wing-body junction. The flow over the wing also separates immediately at the wing leading edge and merges with the vortical flow created from the forebody and the inlet. The spanwise migration of these vortices

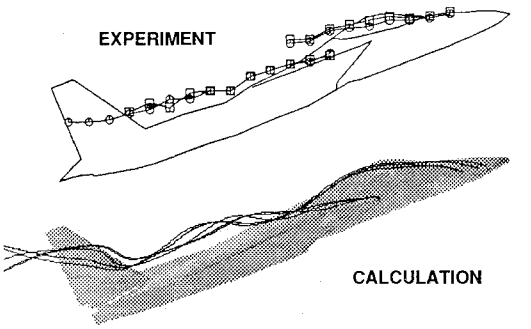

Fig. 8 Particle trajectories for flow over an F-15 wing-body-inlet configuration at $M_\infty = 0.15$ and $\alpha = 20$ deg (side view).

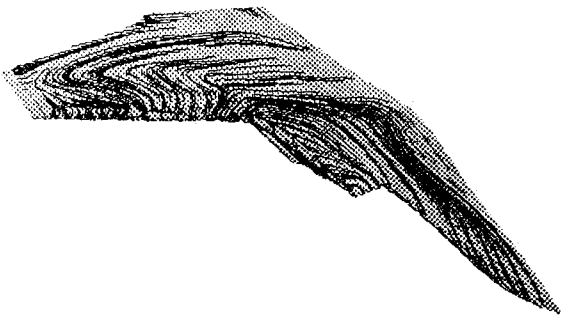

Fig. 9 Surface oil flow visualization of the flow over an F-15 wing-body-inlet configuration.

as well as their liftoff are clearly seen in these figures. All the predicted flow features described above compare well with the experimental results. Figure 9 shows the surface oilflow visualization of the flow over the wing-body-inlet analysis, giving additional details of the separation lines over the wing, inlet, and fuselage.

Figure 10 shows the time history of the sectional loads over the wing at several spanwise stations for the wing-body-inlet combination discussed above. The results are presented for a period of time the aircraft travels several fuselage lengths. As in the wing-alone analysis, distinct, periodic oscillations in the sectional loads are again evident. It appears that one fundamental low frequency and multiple higher frequencies are superimposed. The low-frequency content becomes more dominant toward the wing tip. Thus, the low-frequency oscillations seem to be related more to the flow behavior over the wing than that of the fuselage and inlet. At the fuselage and inlet sections the low-frequency flow behavior is much weaker than on the wing. Thus, the flow separation and vortex shedding associated with the fuselage forebody, inlet, and gun bump are the main source of the high-frequency flow feature.

A Fourier transform of the load history shown in Fig. 10 reveals that the low-frequency content is about 5 Hz and the high frequency stays between 29 Hz at the fuselage and inlet and 34 Hz approaching the wing tip. Experimental studies have been carried out for the identical wing-body-tail configuration at Georgia Tech by Komerath and his co-workers.[9] Their hot wire anemometer measurements showed flow unsteadiness at 7 Hz at the inboard stations, when their model size and tunnel speed were scaled up to the full-scale model and freestream velocities.

A velocity vector plot on a crossflow plane at a distance 80% of the fuselage from the nose is compared with the experiment[8] in Fig. 11. The plane is where the vertical tail leading edge is located. The velocities are interpolated from the calculated flowfield and shown at the measurement locations for one-to-one comparison. It is observed that the location of vortex core and the strength of the vortex compare well with the experiment. However, the predicted shape of the vortex core is slightly flatter and spread in span than that of the experiment.

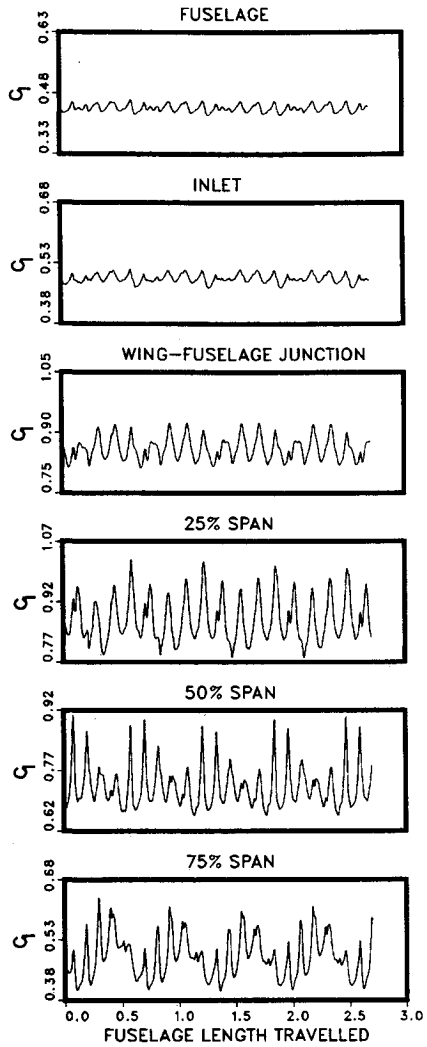

Fig. 10 Variation of sectional lift coefficients with time for an F-15 wing-body-inlet configuration at $M_\infty = 0.15$ and $\alpha = 20$ deg.

Vertical Stabilizer Calculations

The large vortical field over the wing-fuselage-inlet and the associated unsteadiness at high angle-of-attack flight may have detrimental effects on control surfaces such as the vertical tail. As shown earlier in Figs. 7, 8, and 11, the vertical tail is completely submerged in the wake and the core of the vortical flow over the wing-fuselage-inlet is closely located near the midspan of the vertical tail. The vertical tail is strongly influenced by the vortical field so that the airloads at each section have non-negligible values.

To get an order of magnitude estimate of the mean airloads (side forces) that may occur on the vertical tail, calculations were carried out for the F-15 vertical tail placed in the wake of an F-15 wing-body-inlet combination for the wing-body-inlet flight condition discussed above (freestream Mach number of 0.15 and aircraft angle of attack of 20 deg). The angle of attack of the vertical tail relative to the freestream was approximately zero. This requires a two-step analysis. First the wing-body-inlet calculation is done ignoring the vertical tail. Once the wing-body-inlet analysis is completed as discussed earlier, the flow velocity at each grid point on a plane coincident with the vertical tail is obtained by interpolating the wing-body-inlet velocity field from the known vertical tail coordinates in the wing-body-inlet grid system. The second step is to perform a vertical tail-alone Navier-Stokes analysis with the velocities from the first step applied as transpiration boundary conditions at the tail surface. This approach is similar to the method used to study the helicopter blade-wake vortex interactions where the effect of the helical wake on the rotor blade is obtained independently and modeled as an induced velocity distribution over the blade surface.[4] This method only gives a first estimate of the wake-induced airloads on the vertical tail, and the presence of the vertical tail is not included in the wing-body-inlet analysis.

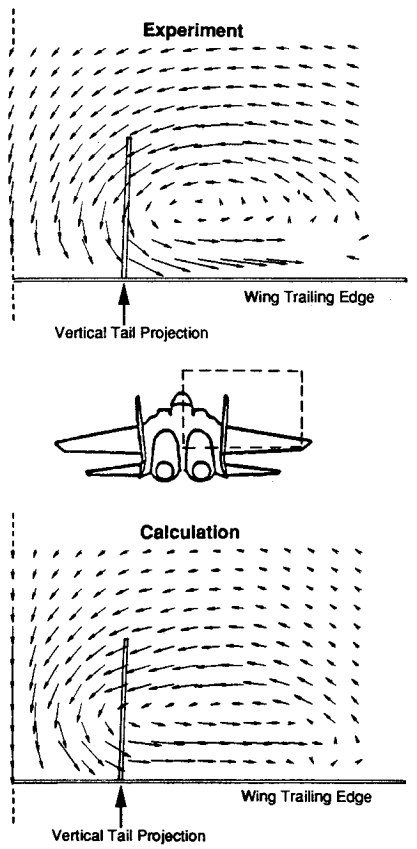

Fig. 11 Details of the vortical flow in the vicinity of the vertical tail.

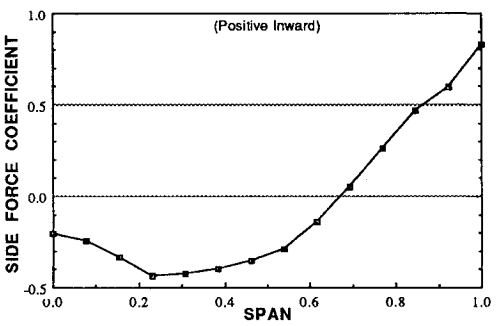

Fig. 12 Side force distribution over the F-15 vertical tail.

Figure 12 shows the airloads over the tail. Note that at the tip of the vertical tail, the side forces are directed inboard,while at the root, the side loads are directed outboard. This is expected because the core of the vortex is located near the midspan of the vertical tail, as seen in Fig. 11.

Conclusions

A computer code capable of solving the three-dimensional, compressible, unsteady, Navier-Stokes equations has been developed and applied to subsonic flow past fighter wings and wing-body-inlet configurations at high angles of attack. The flow separation and vortex formation over the wing and wing-body-inlet configurations are well predicted. The vortex trajectory and the flowfield for the wing-body-inlet configuration compare well with the experiment.

Both the wing-alone, and wing-body-inlet simulations show unsteady fluctuations in the airloads over the wing surface.

For the wing-body-inlet configuration at a typical Mach number of 0.15 and 20-deg angle of attack, the characteristic frequencies are around 5 and 30 Hz. The low-frequency values are in agreement with hot wire measurements.[9]

The vortical flowfield over the wing-fuselage configuration induces non-negligible effective angle of attack over the vertical tail, which leads to sizeable mean side forces. The present computer code provides a methodology for evaluating the largest values of the side forces that the vertical tail will encounter during subsonic maneuvers.

Acknowledgments

This work was supported by a contract from Robins Air Force Base, Warner Robins, GA. Computer time for a set of preliminary calculations on a coarse grid were provided by A. Sugavanam of IBM Corporation at Dallas, TX. The authors are thankful to John B. Malone of NASA Langley Research Center for providing computer resources for the calculations presented here.

References

[1]Thomas, J. L., Walters, R. W., Reu, T., Ghaffari, F., Weston, R. P., and Luckring, J. M., "A Patched Grid Algorithm for Complex Configurations Directed Toward the F/A-18 Aircraft," AIAA Paper 89-0121, Jan. 1989.

[2]Schiff, L. B., Cummings, R. J., and Sorenson, R. L., "Numerical Simulation of High Incidence Flow over the F-18 Fuselage Forebody," AIAA Paper 89-0339, Jan. 1989.

[3]Ruo, S. Y., and Sankar, L. N., "Euler Calculations for a Wing-Alone Configuration," *Journal of Aircraft*, Vol. 25, No. 5, pp. 436–441.

[4]Wake, B. E., and Sankar, L. N., "Solutions of the Navier-Stokes Equations for the Flow About a Rotor Blade," *Journal of the American Helicopter Society*, Vol. 34, No. 2, 1989, pp. 13–23.

[5]Srivastava, R., Sankar, L. N., Reddy, T. S. R., and Huff, D. L., "Application of an Efficient Hybrid Scheme for Aeroelastic Analysis of Advanced Propellers," AIAA Paper 90-0028, Jan. 1990.

[6]Sankar, L. N., and Kwon, O. J., "High-Alpha Simulation of Fighter Aircraft," High-Angle-of-Attack Technology Conf., NASA Langley Research Center, Oct. 30–Nov. 1, 1990.

[7]Anderson, D. A., Tannehill, J. C., and Pletcher, R. H., *Computational Fluid Mechanics and Heat Transfer*, McGraw-Hill, New York, 1984, pp. 549–550.

[8]Komerath, N. M., McMahon, H. M., Schwartz, R. J., Liou, S. G., and Kim, J.-M., "Flowfield Measurements near a Fighter Model at High Angles of Attack," AIAA Paper 90-1431, June 1990.

[9]Komerath, N. M., Schwartz, R. J., Percival, S., and Kim, J.-M., "Unsteady Vortex Flow over Twin-Tailed Aircraft at High Angles of Attack," AIAA Paper 91-0279, Jan. 1991.